Article Identifier
DOI: 10.22032/dbt.58888
URN: urn:nbn:de:gbv:ilm1-2023isc-060:2

60th ILMENAU SCIENTIFIC COLLOQUIUM
Technische Universität Ilmenau, 4 – 8 September 2023
URN: urn:nbn:de:gbv:ilm1-2023isc:1

THEORETICAL CONSIDERATIONS ON 3D TENSEGRITY JOINTS FOR THE USE IN MANIPULATION SYSTEMS

David Herrmann[1], Leon Schaeffer[1], Lena Zentner[2], Valter Böhm[1]

[1]OTH Regensburg, Faculty of Mechanical Engineering, [2]TU Ilmenau, Faculty of Mechanical Engineering

ABSTRACT

This paper presents a comprehensive analysis of a three-dimensional compliant tensegrity joint structure, examining its actuation, kinematics, and response to external loads. The study investigates a baseline configuration and two asymmetric variants of the joint. The relationship between the shape parameter and the parameters of the tensioned segments is derived, enabling the mathematical description of cable lengths for joint actuation. Geometric nonlinear static finite element simulations are performed to analyze the joint's response under various load conditions. The results reveal the joint's range of motion, the effect of different stiffness configurations, and its deformation behavior under external forces. The study highlights the asymmetric nature of the joint and its potential for targeted motion restriction. These findings advance the general understanding of the behavior of the considered tensegrity joint and provide valuable insights for their design and application in soft robotic systems.

Index Terms - Tensegrity Joint, Soft Robotics

1. INTRODUCTION

Soft tensegrity structures, based on highly elastic materials, correspond to a special class of mechanically prestressed structures. They are formed by a set of disconnected compressed segments connected with a continuous net of compliant tensioned segments. The resulting shape of these structures is defined by the prestress. Soft robots based on these structures offer several advantageous properties, such as foldability and deployability, low mass, high strength-to-weight ratio, and shock-absorbing capabilities [1]. These structures have a pronounced ability to change both shape and stiffness. In the last years, there has been an increasing interest in the research of robotic systems based on these structures.

The development of tensegrity-based mobile robots and manipulation systems [2]-[6] is a current research topic. In many corresponding applications, such as in worm-like locomotion systems, fish robots, and manipulation systems based on cascaded structures, the shape-change ability and the actuation are realized by using tensegrity joints [7]-[10]. To realize articulated joints based on tensegrity, biological inspirations (bird neck, human wrist, shoulder or hand) are used or two elementary identical structural units are cascaded by connecting them by tensioned segments [11]-[13]. In most cases spatial joints are realized by means of spatial tensegrity units consisting of two spatial joint parts. The shape change ability of these robots is superficially limited by the deformation capability of these spatial structures which is restricted by the design of the spatial joint parts. The movement range is limited by collision of the spatial joint parts. When using planar joint parts, the range of motion can potentially be increased.

Furthermore, the design and also the actuation can be kept simple. Due to these advantageous properties, a tensegrity joint based on planar joint components is discussed in this paper.
At the beginning of this paper, the description of the geometry of the compliant tensegrity joint is discussed in Section 2. Section 3 presents a simple actuation option using cables. The associated description of the motion and the range of motion are given in Section 4. The main part of the paper deals with the overall mechanical behavior and the analysis of the resulting joint properties (Section 5). Final conclusions and an outlook on further investigations are given in Section 6. The preliminary theoretical investigations in this paper provide a basis for the further realization of compliant tensegrity manipulators with simple and lightweight design and large workspace.

2. JOINT GEOMETRY IN DEPENDENCE ON THE SEGMENT PARAMETERS

The considered compliant tensegrity joint consists of two rigid compressed segments. The compressed segments, which form V-modules with a height H and a right angle between the straight-line sections of the V-modules, are indirectly connected via tensioned segments as illustrated in Fig. 1. In subsequent analyses, we assume that the compressed segment 0 is fixed and has no degrees of freedom. Furthermore, a symmetrical structure is assumed for the primary analyses, which serves as the baseline configuration. Advanced analyses involve the development of asymmetric structural configurations based on this baseline configuration.
Due to its inherent symmetry, the geometry of the baseline configuration can be described using a single parameter, namely the offset d between the centers of the compressed segment ends. This offset d is influenced by the parameters of the tensioned segments and serves as a characterization of the structure. Fig. 1 shows a schematic representation of the structure with the offset. In the following, the parameter d will be referred to as the shape parameter, expressed in dimensionless form as d^*=d/H.
In the x-y-z reference system, the position vectors of the connection points $\vec{r}_i^{\,j}$ on the segments can be defined by the segment index j (j=0,1) and the point numbering i (i=0,1,2):

$$\vec{r}_i^{\,j} = H \cdot \begin{pmatrix} (1-j)\cdot i/2\cdot(5-3i) \\ j\cdot i/2\cdot(5-3i) \\ j\cdot(i^2-3i+2-d^*)+i/2\cdot(3-i) \end{pmatrix};\ j=0{,}1;\ i=0{,}1{,}2 \qquad (2.1)$$

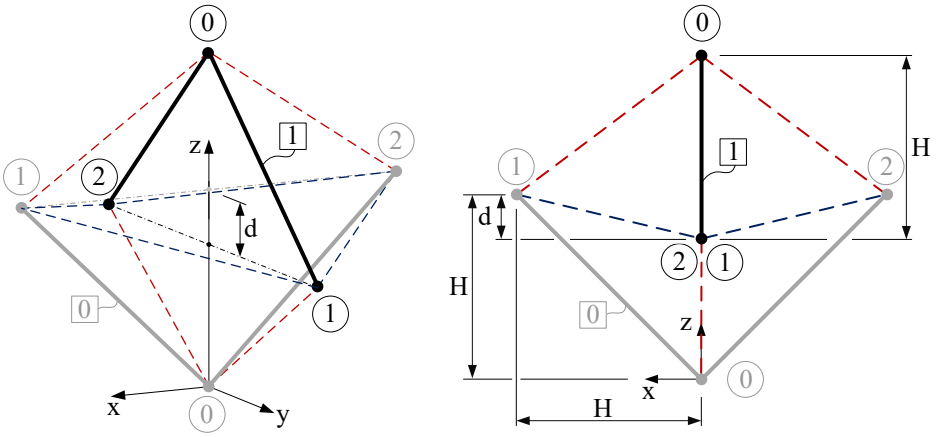

Fig. 1: 3D tensegrity joint with numbering of compressed segments and connection points.

In the following, we investigate the relationship between the shape parameter d^* and the parameters of the tensioned segments. We consider two types of tensioned segments: horizontal tensioned segments (type 1) that connect end points of both compressed segments, and vertical

tensioned segments (type 2) that connect an end point of one compressed segment with a center point of the other compressed segment. The connection points correspond to pin joints. For characterization purposes, we assume that all tensioned segments of each type have the same initial length L_{01}/L_{02} in the undeformed state and the same constant longitudinal stiffness k_1/k_2. At the equilibrium, the lengths of the type 1 L_1 and type 2 L_2 tensioned segments are determined as follows (i,n=0,1,2; j=0,1; m=1-j):

$$L_1 = \left|\vec{r}_i^{\,j} - \vec{r}_n^{\,m}\right| = \sqrt{H^2 + H^2 + d^2} = H \cdot \sqrt{2 + (d^*)^2} \quad \text{where } i \cdot n \neq 0 \tag{2.2}$$

$$L_2 = \left|\vec{r}_i^{\,j} - \vec{r}_n^{\,m}\right| = \sqrt{H^2 + (H-d)^2} = H \cdot \sqrt{1 + (1-d^*)^2} = H \cdot \sqrt{2 + (d^*)^2 - 2d^*} \quad \text{where } i \cdot n = 0 \wedge i + n \geq 1 \tag{2.3}$$

The shape parameter d^* can be determined by analyzing the force equilibrium on a free-cut compressed segment in the considered equilibrium position, since the forces exerted by the tensioned segments on the compressed segment depend on this parameter. Neglecting the weight forces and taking advantage of the symmetry, it is sufficient to examine the equilibrium of forces on a single segment. Each segment is connected to four type 1 tensioned segments between the end points and four type 2 tensioned segments between the end points and the center segment points. We assumed that $L_1 \neq L_{01} \wedge L_2 \neq L_{02}$. Consequently, eight individual forces act on the compressed segment. Considering segment 0, the force acting on connection point i by a tensioned segment between connection points $\vec{r}_i^{\,0}$ and $\vec{r}_n^{\,1}$ of type t (t=1,2; i,n=0,1,2) can be expressed as:

$$\begin{aligned} \vec{F}_t^{0,in} &= k_t(L_t - L_{0t}) \frac{-(\vec{r}_i^{\,0} - \vec{r}_n^{\,1})}{\left|\vec{r}_i^{\,0} - \vec{r}_n^{\,1}\right|} = k_t(L_t - L_{0t}) \frac{-(\vec{r}_i^{\,0} - \vec{r}_n^{\,1})}{L_t} \\ &= k_t \left(1 - \frac{L_{0t}}{L_t}\right)(\vec{r}_n^{\,1} - \vec{r}_i^{\,0}) \end{aligned} \tag{2.4}$$

respectively with the position vectors of the connection points

$$\vec{F}_t^{0,in} = \frac{k_t \cdot H}{2} \cdot \left(1 - \frac{L_{0t}}{L_t}\right) \cdot \begin{pmatrix} -i \cdot (5 - 3i) \\ n \cdot (5 - 3n) \\ -i \cdot (3 - i) - n \cdot (3 - n) + 4 - 2d^* \end{pmatrix} \quad \text{where } t = 1 \text{ for } i \cdot n \neq 0; t = 2 \text{ for } i \cdot n = 0 \wedge i + n \geq 1 \tag{2.5}$$

The forces exerted by the type 1 and type 2 tensioned segments on segment 0 are given by the following equations:

$$\vec{F}_1^{0,in} = k_1 \cdot H \cdot \left(1 - \frac{L_{01}}{H \cdot \sqrt{2 + (d^*)^2}}\right) \cdot \begin{pmatrix} (-3 + 2i) \\ (3 - 2n) \\ -d^* \end{pmatrix} \quad \text{where } i \cdot n \neq 0 \tag{2.6}$$

$$\vec{F}_2^{0,in} = k_2 \cdot H \cdot \left(1 - \frac{L_{01}}{H \cdot \sqrt{2 + (d^*)^2 - 2d^*}}\right) \cdot \begin{pmatrix} -i/2 \cdot (5 - 3i) \\ n/2 \cdot (5 - 3n) \\ 1 - d^* \end{pmatrix} \quad \text{where } i \cdot n = 0 \wedge i + n \geq 1 \tag{2.7}$$

The requirement of the equilibrium of forces on the deformed system $\sum \vec{F} = \vec{0}$ implies that the forces in the x- and y-directions neutralize independently of the parameters due to symmetry. After inserting the forces, the following relationship remains with respect to the z-direction:

$$4k_1 \cdot H \cdot \left(1 - \frac{L_{01}}{H \cdot \sqrt{2 + (d^*)^2}}\right) \cdot (-d^*) + 4k_2 \cdot H \cdot \left(1 - \frac{L_{02}}{H \cdot \sqrt{2 + (d^*)^2 - 2 \cdot d^*}}\right) \cdot (1 - d^*) = 0 \tag{2.8}$$

From equation 2.8, we can finally derive the desired relationship between the parameters of the tensioned segments and the shape parameter d^*, under the condition that $d^* \neq 1$.

$$\frac{d^*}{1 - d^*} \cdot \frac{1 - \frac{L_{01}}{H \cdot \sqrt{2 + (d^*)^2}}}{1 - \frac{L_{02}}{H \cdot \sqrt{2 + (d^*)^2 - 2d^*}}} = \frac{k_2}{k_1} \tag{2.9}$$

In summary, the relationship between the parameters of the tensioned segments and the shape parameter d^* can be expressed as follows, taking into account the lengths L_1 and L_2 of both types of the tensioned segments in the considered equilibrium state.

$$\frac{d^*}{1 - d^*} \cdot \frac{1 - \frac{L_{01}}{L_1}}{1 - \frac{L_{02}}{L_2}} = \frac{k_2}{k_1} \tag{2.10}$$

The analysis of equation 2.10 reveals that the shape parameter of the structure is in the range of $0 < d^* < 1$. This finding is consistent with the results reported in [14].

3. ACTUATION OF THE 3D TENSEGRITY JOINT

To achieve controlled movement of the joint, cable actuation is employed. The cables are overlaid on the tensioned segments of type 2 and extend between a center point and an end point of the compressed segments. The objective of the actuation is to induce rotational movement around a fixed axis of rotation. The following derivation outlines the change in cable length as a function of the segment geometry and the shape parameter d^*. Considering the symmetry of the structure, the length changes apply to both pairs of cables. The neutral position, as illustrated in Fig. 2, exhibits characteristic parameters such as the initial length of the cables L_0 and the angle γ, which denotes the angle formed by the x-axis and the position vector between the axis of rotation and the segment ends.

$$\gamma = \arctan\left(\frac{d}{H}\right) = \arctan(d^*) \tag{3.1}$$

$$L_0 = \sqrt{(H - d)^2 + H^2} = H \cdot \sqrt{(1 - d^*)^2 + 1} \tag{3.2}$$

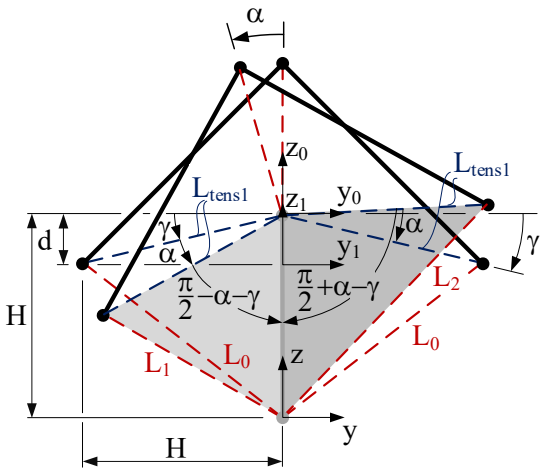

Fig. 2: 2D view of the rotation around the x_1 axis.

From the neutral position, the structure is rotated by a specified angle α to calculate the corresponding cable lengths. In this analysis, we focus on the two triangles marked in gray. The length L_{tens1} of the tensioned segments (type 1) in the two-dimensional view can be determined using the Pythagorean Theorem, as described by equation 3.3. Importantly, this length remains constant for both triangles. The only variation arises in the angle between the length of tensioned segments (type 1) L_{tens1} and the downward compressed segment in the figure due to the rotation.

$$L_{tens1} = \sqrt{d^2 + H^2} = H \cdot \sqrt{(d^*)^2 + 1} \tag{3.3}$$

By applying the law of cosines, the height H of the compressed segment, the length of the tensioned segments (type 1) L_{tens1}, and the angle between them can be used to determine the required cable lengths L_k (k=1,2) as a function of the structural parameters:

$$\begin{aligned} L_k &= \sqrt{L_{tens1}^2 + H^2 - 2 \cdot H \cdot L_{tens1} \cdot \cos\left(\frac{\pi}{2} + (2k-3) \cdot \alpha - \gamma\right)} \\ &= H \cdot \sqrt{(d^*)^2 + 2 + 2 \cdot \sqrt{(d^*)^2 + 1} \cdot \sin\left((2k-3) \cdot \alpha - \arctan(d^*)\right)} \\ &\text{where } k = 1,2 \end{aligned} \tag{3.4}$$

To calculate the changes in length, the initial length of the neutral position L_0 is subtracted from the values obtained.

4. KINEMATICS

Based on the calculated cable lengths and their corresponding actuation, the range of motion of the joint can be described. Initially, we analyze the kinematics, assuming rigid cables and negligible segment weight. Considering the shape parameter d^*, two rotations around non-intersecting axis are identified. The axis of rotation and the associated reference systems are depicted in Fig. 3.

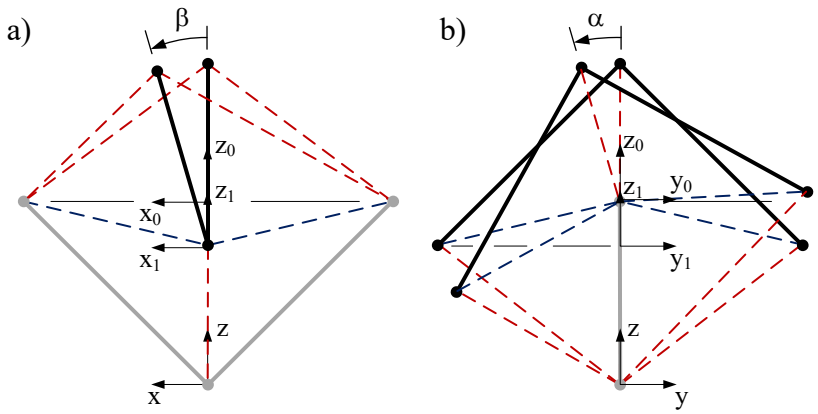

Fig. 3: a) rotation around the y_1-axis (rotation axis 1) by the angle β; b) rotation around the x_0-axis (rotation axis 0) by the angle α.

4.1 Derivation of the position vectors of the connection points of the moving segment

In this subsection, we derive the position vectors of the connection points $\vec{r}_{i,yx}^{\,1}$ in the x-y-z coordinate system. These position vectors are functions of the rotation angle α about rotation axis 0 and the rotation angle β about rotation axis 1. Considering the cascading effect, we must observe the rotation sequence of the structure. With the assumption that the lower joint segment is fixed, the rotation around rotation axis 0 affects the rotation axis 1. Therefore, for mathematical representation, we first perform a rotation around rotation axis 1, followed by a rotation around rotation axis 0. Consequently, the position vectors of the connection points $\vec{r}_i^{\,1,1}$ are established in the reference coordinate system of rotation axis 1, based on the point numbering i (i=0,1,2).

$$\vec{r}_i^{\,1,1} = H \cdot \begin{pmatrix} 0 \\ i/2 \cdot (5-3i) \\ (1-i) \cdot (1-i/2) \end{pmatrix};\ i = 0,1,2 \tag{4.1}$$

The rotation matrix $\boldsymbol{R_y}$ is utilized to rotate the position vector $\vec{r}_i^{\,1,1}$ to a specified coordinate axis. Since the two axes of rotation are offset from each other, the resulting position vector is transformed into the new reference system of rotation axis 0 by subtracting the offset d in the z-direction.

$$\boldsymbol{R_y} = \begin{pmatrix} \cos\beta & 0 & \sin\beta \\ 0 & 1 & 0 \\ -\sin\beta & 0 & \cos\beta \end{pmatrix} \tag{4.2}$$

$$\vec{r}_{i,y}^{\,1,1} = \boldsymbol{R_y} \cdot \vec{r}_i^{\,1,1} \tag{4.3}$$

$$r_{i,y}^{1,0,z} = r_{i,y}^{1,1,z} - d \tag{4.4}$$

The same procedure is repeated for the rotation around rotation axis 0, and the position vector $\vec{r}_{i,yx}^{\,1,0}$ is transformed into the x-y-z coordinate system. Equation 4.8 describes the positions of the considered connection points in terms of the rotation angle, geometry parameters, and connection point numbering.

$$\boldsymbol{R_x} = \begin{pmatrix} 1 & 0 & 0 \\ 0 & \cos\alpha & -\sin\alpha \\ 0 & \sin\alpha & \cos\alpha \end{pmatrix} \tag{4.5}$$

$$\vec{r}_{i,yx}^{\,1,0} = \boldsymbol{R_x} \cdot \vec{r}_{i,y}^{\,1,0} \tag{4.6}$$

$$r_{i,yx}^{1,z} = r_{i,yx}^{1,0,z} + H \tag{4.7}$$

$$\vec{r}_{i,yx}^{\,1} = H \cdot \begin{pmatrix} \sin\beta \cdot \left(1 - \frac{i}{2}\right) \cdot (1 - i) \\ \sin\alpha \cdot \left(d^* - \cos\beta \cdot \left(1 - \frac{i}{2}\right) \cdot (1 - i)\right) + \cos\alpha \cdot \frac{i}{2} \cdot (5 - 3i) \\ 1 - \cos\alpha \cdot \left(d^* - \cos\beta \cdot \left(1 - \frac{i}{2}\right) \cdot (1 - i)\right) + \sin\alpha \cdot \frac{i}{2} \cdot (5 - 3i) \end{pmatrix} \tag{4.8}$$
$$i = 0{,}1{,}2$$

4.2 Analysis of the range of motion

Fig. 4 a) and b) show the workspace of the center point of the moving segment as a point cloud for a shape parameter d^* of 0 and 0.1. The angles α and β were varied from -80° to +80° in 1° increments. To enhance clarity, we removed the data points with no offset from one quadrant. When there is no offset between the compressed segments (d^*=0), the workspace forms a perfect spherical shell. Due to the rotational order of the system, the workspace exhibits symmetry only in the x-z plane and displays a circular section in the x-direction. When there is an offset present in the kinematic motion, the neutral position of the center point is shifted downward by d. Combined with the offset primary axis, this results in a downward-shifted circular arc that is rotated in the x-direction by the fixed rotation axis. Despite this, the characteristic of the workspace remains the same, but its shape is compressed by the rotation around two mutually displaced axis in the y-direction. The result is an ellipsoid instead of a perfect sphere. This observation is depicted in Fig. 4 b).

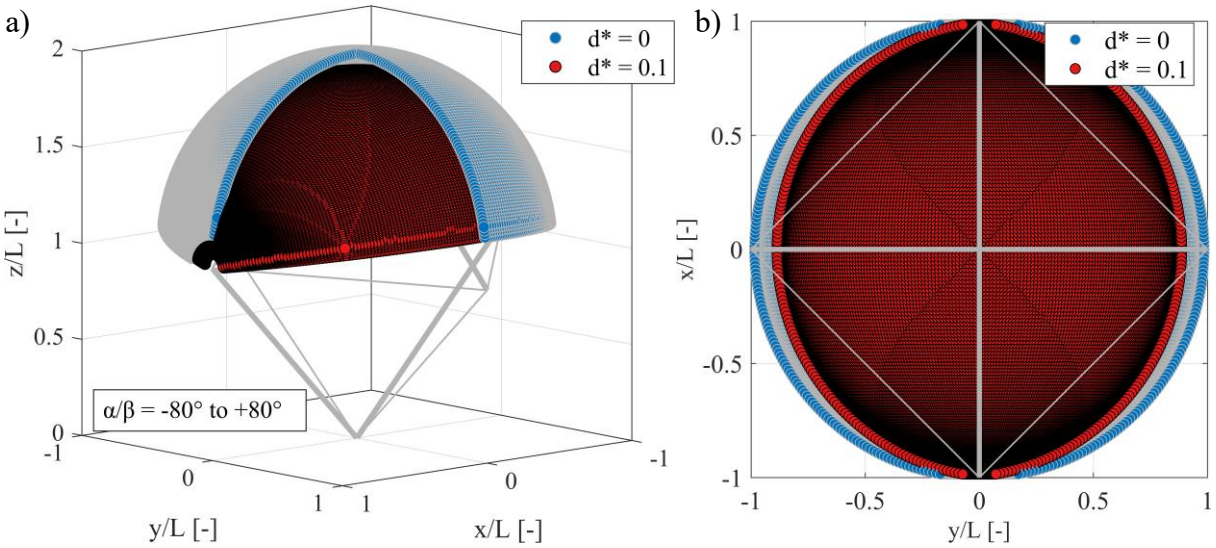

Fig. 4: Range of motion of the tensegrity joint when the angles α and β is varied by ±80°; a): values of the first quadrant removed for better visualization.

5. STIFFNESS CHARACTERIZATION – FLEXIBILITY ELLIPSOIDS

After demonstrating the range of motion of the joint, the flexibility of the joint is examined, which is particularly important for its use as a passive joint. To analyze this, we employed a geometrically nonlinear static finite element simulation using bar elements. The tensioned segments are modeled as low stiffness bars, while the compressed segments are modeled as bars with significantly higher stiffness. The specific parameter values for the base configuration are shown in Table 1. To maintain the shape of the compressed segments, we introduce additional bars. The cables required for joint actuation are either neglected or defined as untensioned in this analysis. Furthermore, the effect of gravity is not taken into account.
The analysis begins by determining the neutral position of the structure using the form-finding algorithm described in [15]. This neutral position remains constant throughout all analyses, with a fixed shape parameter d^* of 0.1. To achieve this, the initial length L_{02} of the tensioned segments of type 2 is adjusted. For the symmetric baseline configuration, the determination is carried out according to equation 5.1, derived from equation 2.10. For the two asymmetric structure variants considered, we determined the initial length L_{02} iteratively.

$$L_{02} = L_2 \cdot \left(\frac{L_{01} \cdot d^* \cdot k_1 - L_1 \cdot d^* \cdot k_1}{L_1 \cdot k_2 - L_1 \cdot d^* \cdot k_2} + 1 \right) \tag{5.1}$$

Once the neutral position is established, external loads are applied to the joint to observe and analyze its response. This paper focuses on two types of loads: a three-dimensional rotational force applied to the center point (0) of the moving segment (1) and two opposing forces applied to the end points (1/2) of the segment. The first load case is accompanied by a parameter study, that investigates the influence of load magnitude and the stiffness of the horizontal tensioned segments of type 1 in the base configuration. In addition, two new joint variants are generated by asymmetrically varying the stiffness of the type 2 bar pairs, and these variants are discussed. Finally, we consider the second load case, representing torsion about the z-axis.

Table 1: Parameters of the basic configuration

Designation	Variable	Value	Unit
Geometric dimensions			
Height of compressed segment	H	100	mm
Shape parameter	d^*	0.1	-
Initial length of tensioned segments (type 1)	L_{01}	130	mm
Initial length of tensioned segments (type 2)	L_{02}	variable	mm
Stiffness of bar elements			
Stiffness of tensioned segments (type 1)	k_1	1	N/mm
Stiffness of tensioned segments (type 2)	k_2	1	N/mm
Stiffness of auxiliary bars	k_{au}	10000000	N/mm
Stiffness of compressed bars	k_{comp}	100000	N/mm

5.1 Three-dimensional external load

To analyze the effect of force magnitude on the joint, we apply two different force values of 30 N and 40 N, and observe the resulting joint reactions in terms of displacement of the center point (0) of the movable segment (1). The direction of the force is determined by two solid angles before each simulation and remains constant throughout the simulation. The force magnitude of 40 N serves as the baseline for subsequent analyses.
The results for the directional variation of the force with a solid angle increment of 10° are shown in Fig. 5. The compressed segments are depicted as thick lines, while the tensioned

segments are represented by thinner lines. The neutral position of segment 1 lies in the x-z plane. In both cases considered, the flexibility ellipsoid exhibits a greater extension in the x-direction compared to the y-direction, indicating that the resistance of the joint to rotation around the axis of rotation 1 (y_1-axis) is lower. This suggests that rotation in this direction is softer or more elastic than rotation around the axis of rotation 0. This observation aligns with the structural design of the joint. In the y-z plane, three tensioned segments limit the movement of the segment endpoints and the rotation axis. Consequently, the applied force acts directly on the lower compressed segments via the upper tensioned segments (type 2). In the x-z plane, however, the actual axis of rotation shifts with respect to the endpoints of the lower compressed segment, resulting in more pronounced deformation.
Comparing the responses to different force magnitudes, it becomes evident that magnitude of the force has a nonlinear influence on the dimensions of the ellipsoid. A larger force leads to larger displacements of the center point in all spatial directions. However, the overall curvature of the ellipsoid is maintained due to the structural characteristics of the joint.

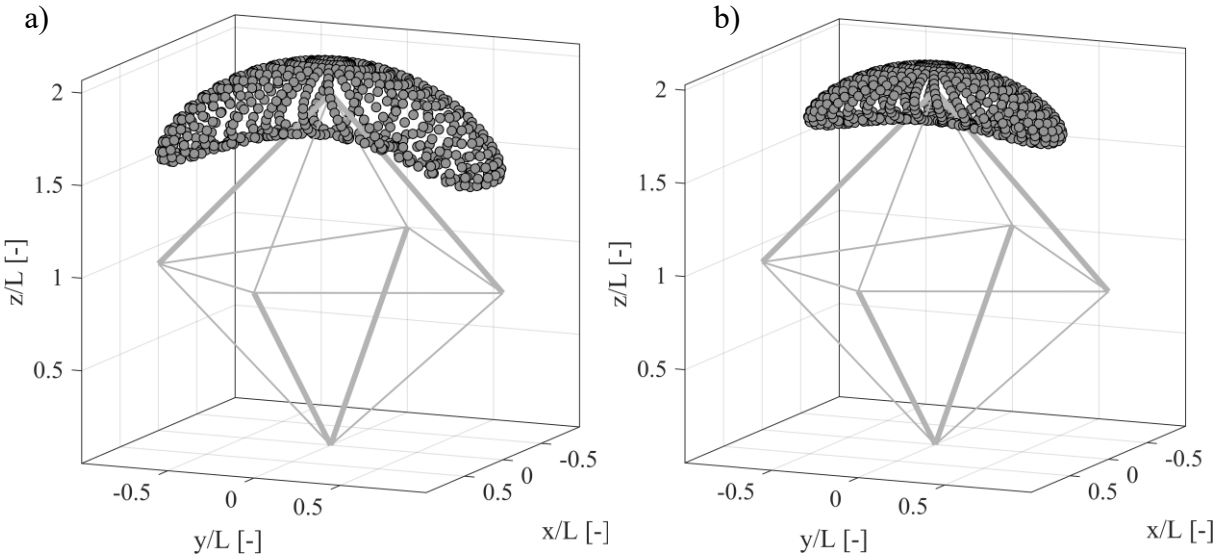

Fig. 5: Flexibility ellipsoids of the center point of segment 1 under a direction-fixed force on the center point of the segment at a force magnitude of 40 N (a) and 30 N (b); solid angle increment: 10°.

To investigate the influence of the stiffness of the horizontal tension segments (type 1) on the flexibility of the joint, the stiffness is increased by a factor of 10 from the baseline configuration, where it was 1 N/mm. In Fig. 6, the effect of the stiffened tension segments on the stiffness of the joint is depicted. The increased stiffness of the tension segments leads to a reduction in the expression of flexibility variation in different spatial directions. The effect of the tension segments on the joint's stiffness is significant. However, the primary characteristic related to the variation of the flexibility of the joint in the x-y plane remains evident. The force magnitude is kept constant at 40 N in both cases.
In the following analysis, two asymmetrical joint variants will be discussed, which deviate from the previously considered symmetrical designs. These variants are characterized by different stiffnesses of the pairs of tensioned segments (type 2), leading to increased resistance forces against specific elementary rotations and further specifying their applications. Fig. 7 illustrates the two asymmetrical configurations along with their corresponding ellipsoids. In configuration a), the stiffness of the two lower tensioned segments is increased by a factor of 10, while in configuration b), the stiffness of the two upper tensioned segments is increased by the same factor. In both cases, the increased stiffness restricts the motion of the joint in the z-direction. This restriction can be attributed to the resulting force direction of the modified tensioned segments. In case a), where we stiffened the two lower segments, the flexibility in the

y-direction is substantially reduced compared to the x-direction. This effect is similarly observed for the upper segments, but in the x-direction. Consequently, by increasing the stiffness of the lower segments, it is possible to achieve a homogenization of the ellipsoid's characteristics in the x-y plane, to the extent that the characteristic may even be reversed. On the other hand, the second asymmetric joint variant enhances the characteristic features of the tensegrity joint, allowing for targeted restriction of movement or rotation along a specific direction depending on the joint position.

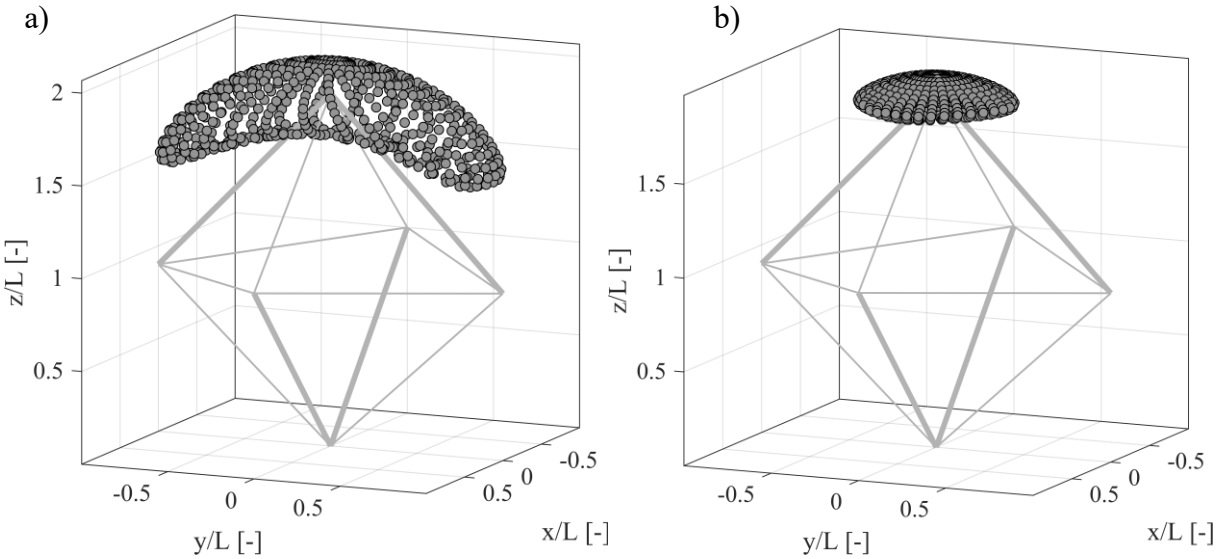

Fig. 6: Flexibility ellipsoids of the center point of segment 1 at a direction-fixed force on the center point of the segment at a stiffness of the tensioned segments (1) of 1 N/mm (a) and 10 N/mm (b); solid angle increment: 10°.

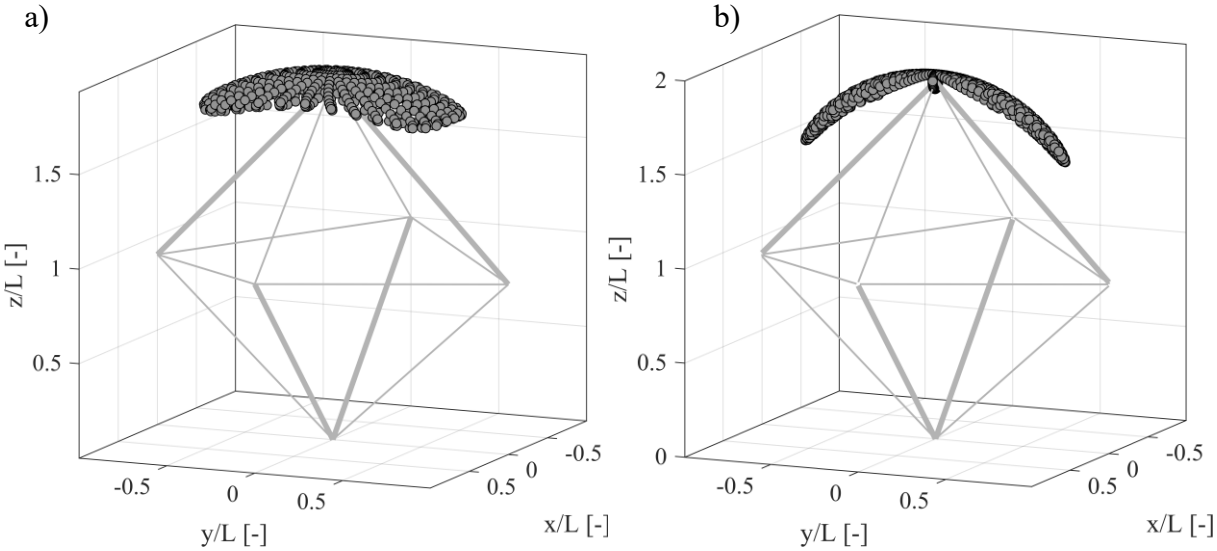

Fig. 7: Asymmetrical joint variants to specifically influence the joint characteristics; a) Stiffness of the lower pair of tensioned segments (type 2) 10 N/mm; b) Stiffness of the upper pair of tensioned segments (type 2) 10 N/mm; solid angle increment: 10°.

5.2 Torsional load

In the second load case, we apply two forces parallel to the x-y plane, acting on the end points of the movable compressed segment 1. These forces are oriented perpendicular to the compressed segment and maintain this orientation throughout the simulation, resulting in a consistent torsional moment around the z-axis. We conduct the analysis with the basic configuration, and incrementally increase the force magnitude to examine the deformation

behavior. The displacements of the three connection points of the movable segment are illustrated in Fig. 8.
Regarding the center of the compressed segment, a displacement in the negative z-direction is observed as the torsional moment increases. This behavior can be likened to that of a screw, as the joint structure translates the applied plane load into the third dimension. In terms of static stability, it is noted that the force can be increased up to a magnitude of 50.6 N. Beyond this point, the finite element simulation fails to converge to a solution. This limitation can be attributed to the idealized nature of the joint, which does not account for contact interactions between components. Therefore, we presume that larger rotations can be achieved during experimental validation.

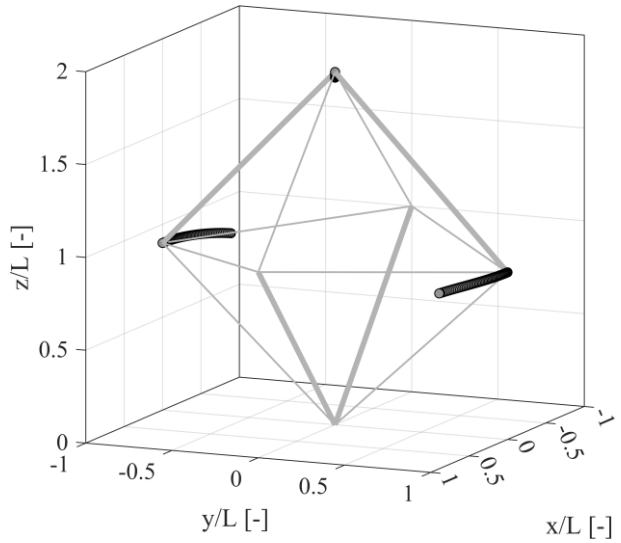

Fig. 8: Trajectories of the connection points of the moving segment 1 with torsional force variation.

6. CONCLUSION

This paper presented a comprehensive investigation of a three-dimensional compliant tensegrity joint, encompassing its geometry, actuation, kinematics, and flexibility. The geometry of the joint was described by a single parameter, the shape parameter d^*, over different configurations. A simple cable actuation method was presented, along with its mathematical representation. Analysis of the range of motion reveals a spherical shell shape when $d^* = 0$, and a compressed ellipsoid along the moving axis when $d^* \neq 1$. The stiffness of the joint was characterized by flexibility ellipsoids, demonstrating significant variations in different spatial directions in the basic configuration. By employing asymmetric variants, the characteristic of the joint can be selectively adjusted, leading to homogenization or restricted motion/rotation in specific directions. Additionally, the joint exhibits displacement along the moment axis under torsional loads. Future research aims to experimentally validate the joint's characteristics. Furthermore, dynamic analyses are planned to determine its application limits and segment parameterization for future applications. These findings will contribute to the development of compliant manipulators tailored to specific application requirements.

ACKNOWLEDGEMENTS

The authors gratefully acknowledge the support of the Deutsche Forschungsgemeinschaft (DFG, German Research Foundation) through Priority Program SPP 2100 "Soft Material Robotic Systems" (Projects BO4114/3-2, ZE714/14-2).

REFERENCES

[1] J. Rieffel, and J.-B. Mouret, “Adaptive and Resilient Soft Tensegrity Robots,” Soft Robotics, Vol. 5, No. 3, pp. 318–329, 2018. doi: 10.1089/soro. 2017.0066.

[2] M. Vespignani, J. M. Friesen, V. SunSpiral, and J. Bruce, “Design of SUPERball v2, a Compliant Tensegrity Robot for Absorbing Large Impacts,” in 2018 IEEE/RSJ International Conference on Intelligent Robots and Systems (IROS), Madrid, pp. 2865–2871, 2018. doi: 10.1109/IROS.2018.8594374.

[3] Y. Lu, X. Xu, and Y. Luo, “Path Planning for Rolling Locomotion of Polyhedral Tensegrity Robots Based on Dijkstra Algorithm,” Journal of the International Association for Shell and Spatial Structures, Vol. 60, No. 4, pp. 273–286, 2019. doi: 10.20898/j.iass.2019.202.037.

[4] K. Kim, A. K. Agogino, and A. M. Agogino, “Rolling Locomotion of Cable-Driven Soft Spherical Tensegrity Robots,” Soft Robotics, Vol. 7, No. 3, pp. 346–361, 2020. doi: 10.1089/soro.2019.0056.

[5] P. Schorr, F. Schale, J. M. Otterbach, L. Zentner, K. Zimmermann, and V. Boehm, “Investigation of a Multistable Tensegrity Robot applied as Tilting Locomotion System,” in 2020 IEEE International Conference on Robotics and Automation (ICRA), Paris, pp. 2932–2938, 2020. doi: 10.1109/ICRA40945.2020.9196706.

[6] D. Fadeyev, A. Zhakatayev, A. Kuzdeuov, and H. A. Varol, “Generalized Dynamics of Stacked Tensegrity Manipulators,” IEEE Access, Vol. 7, pp. 63472–63484, 2019. doi: 10.1109/ACCESS.2019.2916681.

[7] J. Shintake, D. Zappetti, T. Peter, Y. Ikemoto, and D. Floreano, “Bio-inspired Tensegrity Fish Robot,” in 2020 IEEE International Conference on Robotics and Automation (ICRA), Paris, pp. 2887–2892, 2020. doi: 10.1109/ICRA40945.2020.9196675.

[8] V. Böhm, P. Schorr, F. Schale, T. Kaufhold, L. Zentner, and K. Zimmermann, “Worm-Like Mobile Robot Based on a Tensegrity Structure,” in 2021 IEEE 4th International Conference on Soft Robotics (RoboSoft), New Haven, pp. 358–363, 2021. doi: 10.1109/RoboSoft51838.2021.9479193.

[9] S. Lessard, D. Castro, W. Asper et al., “A bio-inspired tensegrity manipulator with multi-DOF, structurally compliant joints,” in 2016 IEEE/RSJ International Conference on Intelligent Robots and Systems (IROS), Daejeon, pp. 5515–5520, 2016. doi: 10.1109/IROS.2016.7759811.

[10] B. Fasquelle, M. Furet, P. Khanna, D. Chablat, C. Chevallereau, and P. Wenger, “A bio-inspired 3-DOF light-weight manipulator with tensegrity X-joints,” in 2020 IEEE International Conference on Robotics and Automation (ICRA), Paris, pp. 5054–5060, 2020. doi: 10.1109/ICRA40945.2020.9196589.

[11] V. Ramadoss, K. Sagar, M. S. Ikbal, J. H. L. Calles, R. Siddaraboina, and M. Zoppi, “HEDRA: A Bio-Inspired Modular Tensegrity Robot With Polyhedral Parallel Modules,” in 2022 IEEE 5th International Conference on Soft Robotics (RoboSoft), Edinburgh, pp. 559–564, 2022. doi: 10.1109/RoboSoft54090.2022.9762130.

[12] B. Fasquelle, M. Furet, C. Chevallereau, and P. Wenger, “Dynamic modeling and control of a tensegrity manipulator mimicking a bird neck,” in: Uhl, T. (eds) Advances in Mechanism and Machine Science. IFToMM WC 2019. Mechanisms and Machine Science, Vol. 73, Springer, Cham, pp. 2087–2097, 2019. doi: 10.1007/978-3-030-20131-9_207.

[13] D. Zappetti, R. Arandes, E. Ajanic, and D. Floreano, “Variable-stiffness tensegrity spine,” Smart Materials and Structures, Vol. 29, No. 7, Paper-ID: 075013, 2020. doi: 10.1088/1361-665X/ab87e0.

[14] V. Böhm, A. Jentzsch, T. Kaufhold, F. Schneider, F. Becker, and K. Zimmermann, “An approach to locomotion systems based on 3D tensegrity structures with a minimal number of struts,” in 7th German Conference on Robotics, Munich, pp. 150–155, 2012.
[15] V. Böhm, S. Sumi, T. Kaufhold, and K. Zimmermann, “Compliant Multistable Tensegrity Structures,” Mechanism and Machine Theory, Vol. 115, pp. 130–148, 2017. doi: 10.1016/j.mechmachtheory.2017.04.013.

CONTACTS

David Herrmann M.Sc. email: david.herrmann@st.oth-regensburg.de
Leon Schaeffer M.Sc. email: leon.schaeffer@oth-regensburg.de
Prof. Dr.-Ing. habil. Lena Zentner email: lena.zentner@tu-ilmenau.de
Prof. Dr.-Ing. habil. V. Böhm email: valter.boehm@oth-regensburg.de

